VICTORIA UNIVERSITY
MELBOURNE AUSTRALIA

Road vehicle shock detection algorithm using the Hilbert envelope

This is the Published version of the following publication

Road vehicle shock detection algorithm using the Hilbert envelope

V. Rouillard [*], M.J. Lamb

Engineered Packaging and Distribution Research Group, Victoria University, Melbourne, Australia, PO Box 14428, MCMC 8001 Melbourne, Australia

A B S T R A C T

Detecting and characterising shocks is challenging because they do not occur in isolation but are instead superimposed onto underlying vehicle vibrations which themselves are a result of the interaction with uneven road surfaces. Consequently, shocks are buried within vehicle vibration response measurements (usually acceleration). This paper presents the development and validation of an automated algorithm to detect shocks from vertical acceleration signals measured from road vehicles. To avoid inherent difficulties with experimentation, this initial paper is confined to numerical simulation whereby the response of two typical quarter-car truck models (one with air ride and the other with steel suspension) when travelling on artificially-generated random road elevation profiles laced with Hanning-shaped surface aberrations of known amplitude, lengths and location along the elevation profile. The shock detection algorithm was developed as a dual mode classifier to accommodate the two natural frequencies of each 2DoF quarter car models. Detection was implemented by first passing the vibration response signal through a band-pass filter around the two resonant modes in turn then calculating the filtered signals' instantaneous frequency (envelope) by means of the Hilbert transform. Shock detection was based on the local peak-to-mean ratio (LPTMR) of the instantaneous magnitude where 'local' was defined by the duration of the filtered signal's impulse response function. Sensitivity analysis and validation were undertaken on artificially-generated roads of varying roughness onto which aberrations of known shape were superimposed. The effectiveness and limitations (detection threshold) of the algorithm were evaluated by creating a range of aberrations with a broad range of lengths (effective frequencies) and diminishing amplitudes. Results show that shocks of 'significant' magnitudes are always detected with no detection of false positives. As the road roughness increases relative to the aberration amplitudes, the resulting shocks become increasingly drowned-out by the vibration response due to the underlying road roughness, especially for the quarter-car model with steel suspension. The main conclusion is that the signal analysis approach taken is ultimately effective and needs to be further validated using experimental response data.

1. Introduction

The ability to detect of shocks generated when road vehicles encounter road surface aberrations is important and challenging. It has long been recognized that these shocks are one of the main causes of product damage resulting in excessive packaging. In addition,

* Corresponding author.
  E-mail address: vincent.rouillard@vu.edu.au (V. Rouillard).

severe shocks adversely affect ride quality which is especially important for patient transport as well as a potential source of damage to vehicles. The impulse-like character of shocks often contains a wide range of frequencies and, as such, tend to induce significant response in the product that often lead to product damage [1–4]. Shocks during transport may well be the difference between shipments reaching their destination unscathed or in a damaged condition. Despite this, shocks, unlike vibrations, are seldom included in laboratory-based transport tests such as those undertaken in accordance with standard methods published by ASTM, ISO, and ISTA. This shortcoming is due to two main reasons: (1) that the identification of and the extraction of important information (such as shape, duration and magnitude) on shocks buried within random vibration signals is challenging [5,6] and (2) the difficulties with faithfully reproducing shock-on-random vibrations on standard vibration test systems.

For realistic simulation of road vehicle shock and vibrations to be achievable, a method by which shocks buried within road vehicle vibration signals can be detected and characterised needs to be developed and validated.

2. Literature review

Because shocks cannot be analysed with techniques used for random vibrations, any shock present within the signal measured from road vehicles must first be extracted from the underlying vibrations. This task is challenging because both events are measured concurrently with the same device (usually an accelerometer) and both are co-manifested within one signal. To make matters more difficult, the definition of shocks and transients is not simple. Some examples include "*a temporarily sustained vibration of a mechanical system. It may consist of forced or free vibration or both*" [7]; "*Transients … physically exist only within a finite, measurable time interval, that is, where the input process and the output process have nonzero values…*" [7]; and "*The transient response refers to that portion of the response due to the closed-loop poles of the system…*" [8]. In other words, transients are defined as a vibration composed of the vehicle's impulse response (transfer function poles) caused by a short duration and finite excitation.

Recent reviews on shock detection [9,10] reveal that a number of attempts have been made at detecting shocks during road transport. These make use of the moving crest factor [11] (albeit on road profiles), Intrinsic Mode Functions [12,13], the Wavelet transform [14–16] and the Hilbert-Huang transform [17–19]. These methods, along with others such as the crest factor, were reviewed and evaluated by Lepine et al. [20] who showed that, to date, there is no single method which can reliably identify the various components of random vehicle vibrations. Lepine [20] reviewed a Machine Learning application for the detection of shocks by Mednis et al. [21] and developed an enhanced Machine Learning approach that combined 36 processed signals (predictors) using the crest factor, rms, kurtosis, the wavelet transform, and the Hilbert-Huang transform to yield promising detection performances (precision, accuracy and recall) [20]. Lepine [20] subsequently tested the accuracy of the new Machine Learning shock detection algorithm on field data using a four-wheeled vehicle travelling on a test track containing a number of carefully positioned obstacles. This yielded encouraging results (especially in the detection of larger, more significant, shocks) but revealed that further enhancement of the algorithms is required to reliably detect smaller shocks from multi-wheeled vehicles. More recently, further applications of Machine Learning to detect shocks have been undertaken [22–25] but these remained to be thoroughly validated for road transport vehicles. A further limitation of Machine Learning based techniques is the requirement to train the algorithms for specific transport configurations. An alternative approach to detect road surface defects was proposed by [26–28] by evaluating the load paths through the suspension system of a numerical quarter-car model given road elevation data. Although useful in its approach, the method relies of a having access to road elevation data as well as accurate information on the vehicle's dynamic parameters and does not lend itself to shock detection from vibration response measurements.

3. Method

This paper presents the development and validation of an automated algorithm designed to detect the presence of shocks from vertical acceleration signals measured from road vehicles without the need to first train the algorithm. To avoid time-consuming physical experiments, a numerical approach was used to develop and validate the algorithm in the first instance; physical validation will be undertaken in the future.

The numerical approach involves the creation of artificial random road profiles laced with introduced surface aberrations at known locations along the profile. The vibration response of an idealised vehicle model when travelling on the artificial road at speed will then be calculated. As a first step, especially to circumvent complexities associated with the response of multi-wheeled vehicles, the initial work will use a linear quarter-car vehicle model to compute the vertical acceleration response of the sprung mass. The vehicle models used were configured to represent typical road transport vehicles with steel leaf and air suspension types.

Broadly, the approach requires that the following be carried-out:

1. Establishing the dynamic characteristics of typical quarter-car models
2. The creation / synthesis of realistic road elevation profiles
3. The synthesis of road surface aberrations of predetermined shapes, lengths and amplitudes
4. The superposition of the road surface aberrations at known locations onto the synthesized road profile
5. The calculation of vehicle response (sprung mass heave acceleration) from the interaction with the synthesized road profile with added aberrations
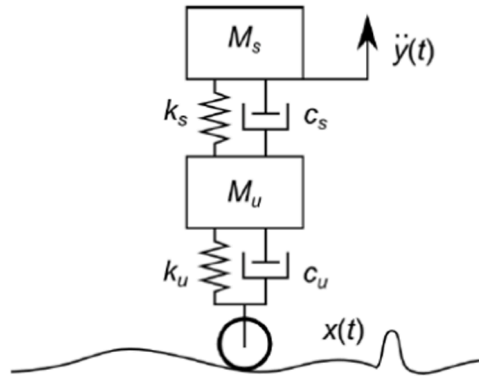6. The evaluation and optimisation of the shock detection algorithm
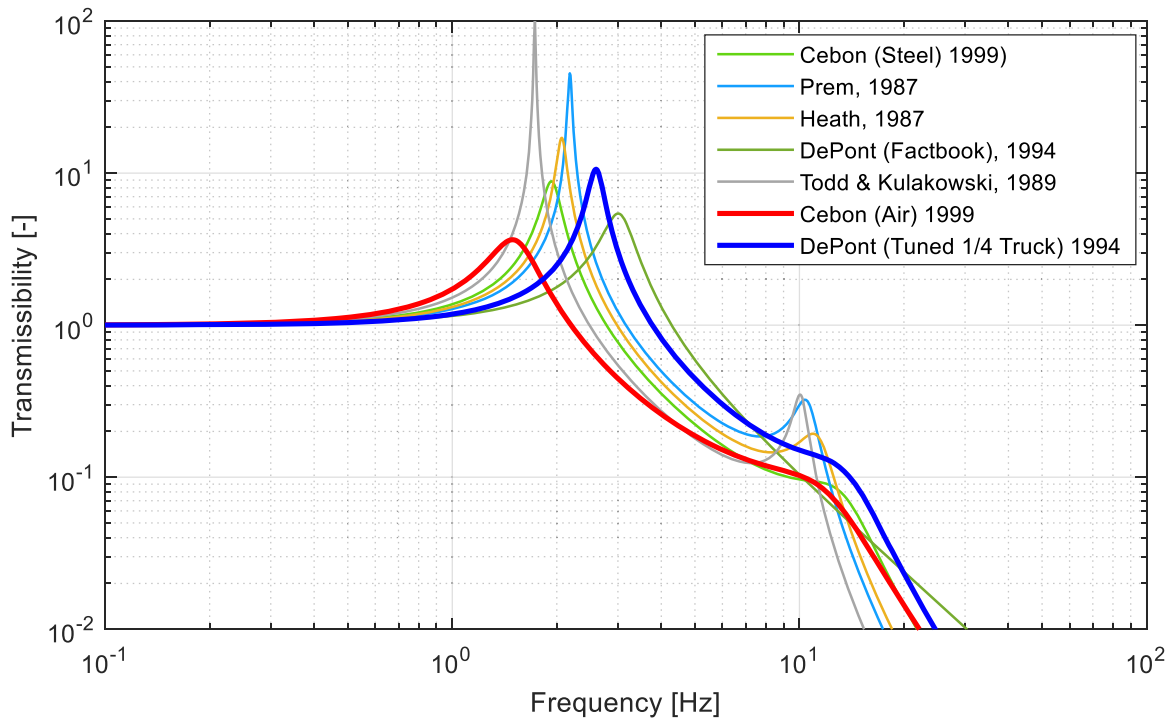
Fig. 1. Quarter-car vehicle model.

Fig. 2. Magnitude FRF of a range of published quarter-car models.

4. Quarter car response to uneven surfaces

A useful and popular approach to studying vehicle dynamics is to use the quarter-car model [29] which, due to its simplicity, only accounts for motion in the vertical direction. Further simplification is afforded by assuming linearity of the damping and stiffness coefficient. The quarter-car can be thus easily modelled as a two degree-of-freedom (DoF) system with a set of simple differential equations that can be solved numerically to produce the vertical motion of the sprung mass for any arbitrary displacement excitation (road elevation profile) at the wheel/road interface as shown in Fig. 1.

4.1. Quarter-car model frequency response function

Neglecting the influence of tyre damping, the magnitude frequency response function (FRF) - transmissibility - of a linear quarter-car (two DoF system) is described, in the Laplace domain, by:

Table 1
ISO-8608 road class degrees of roughness.

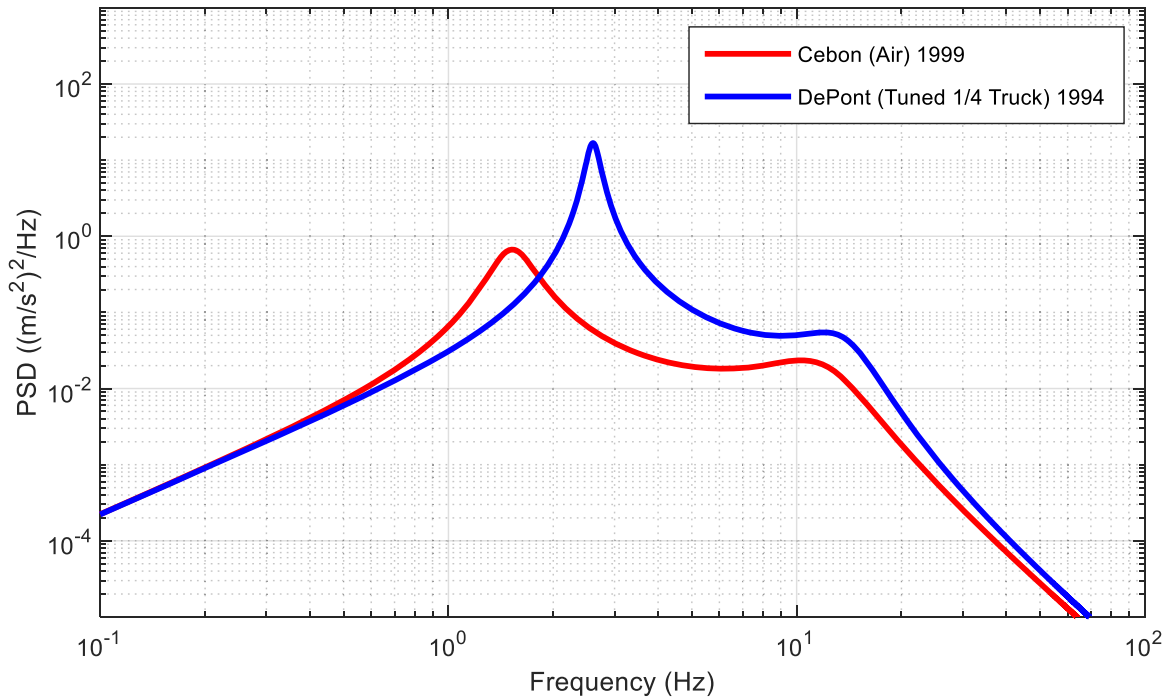| Road class	$G_d(\Omega_o)$ [10^{-6} m³/rad]		
	Lower limit	Mean	Upper limit
A	–	1	2
B	2	4	8
C	8	16	32
D	32	64	128
E	128	256	512
F	512	1024	2048
G	2048	4096	8192
H	8192	16,384	32,768

$\Omega_o = 1$ rad/m.

Fig. 3. Acceleration response PDS of two representative quarter –car vehicle models travelling on a class B road at 80 km/h.

$$|FRF| = \left| \frac{\omega_{n,u}^2 \left(2\zeta_s \omega_{n,s} s + \omega_{n,s}^2 \right)}{\left(s^2 + 2\rho\zeta_s\omega_{n,s}s + \omega_{n,u}^2 + \rho\omega_{n,s}^2 \right)\left(s^2 + 2\zeta_s\omega_{n,s}s + \omega_{n,s}^2 \right) - \rho\left(2\zeta_s\omega_{n,s}s + \omega_{n,s}^2 \right)^2} \right| \tag{1}$$

where,

$\omega_{n,s}$ and $\omega_{n,u}$ are the decoupled sprung and unsprung mass natural frequencies in rad/s respectively, $\omega_{n,s} = \sqrt{\frac{k_s}{m_s}}$ and $\omega_{n,u} = \sqrt{\frac{k_u}{m_u}}$, ζ_s is the decoupled sprung mass damping ratio: $\zeta_s = \frac{c_s}{2m_s\omega_{n,s}}$ and $\rho = \frac{m_s}{m_u}$, where m_s and m_u are the sprung and unsprung masses, respectively. ω is the excitation frequency in rad/s, $s = \pm i\omega$ is the Laplace operator.

Numerical quarter-car models representing typical vehicles using realistic mass, damper and stiffness values for transport vehicles have been developed by a number of experts in the field [29–33]. The magnitude FRFs for a selection of such quarter-car models are shown graphically in Fig. 2. This reveals the presence of two natural frequencies representing the two modes of vibration expected of a two DoF system namely the sprung and unsprung mass resonances. For the purpose validating the shock detection algorithm, two representative models representing a variety of vehicle types were selected: Cebon [30] for air suspension and DePont [31] for steel leaf suspension.
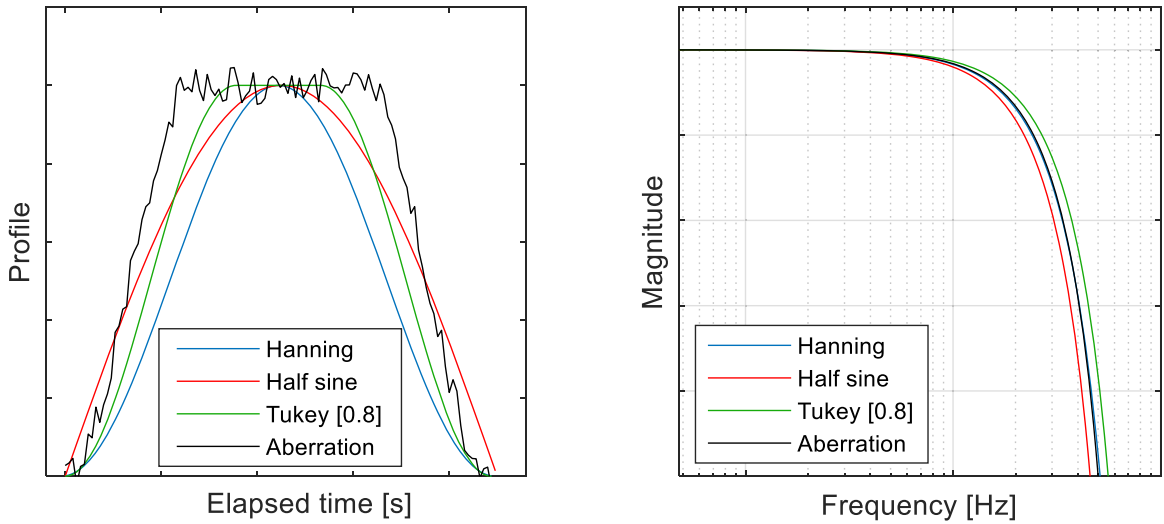
Fig. 4. Mathematical aberration shapes along with a typical (synthesized) aberration and corresponding frequency spectra.

4.2. Quarter car response to random (road surface) excitation

4.2.1. Road profile models and synthesis

The excitation to a vehicle when travelling at constant speed on a typical road is simulated using a random elevation road profile with a Power Density Spectrum (PDS) described by:

$$G_d(\Omega) = G_d(\Omega_o) \cdot (\Omega/\Omega_o)^{-2} \tag{2}$$

, where Ω is the angular spatial frequency in rad/m and $G_d(\Omega_0)$ the overall road roughness coefficient as described in Table 1 [34] for various road classes.

The acceleration response PDS of a quarter-car can be easily computed by first transforming the spatial road elevation spectrum (1) into a temporal road elevation spectrum, $G_d(\omega)$ by applying a constant vehicle speed, v:

$$G_d(\omega) = \frac{1}{v} \cdot G_d(\Omega_o) \cdot \left(\frac{\Omega}{\Omega_o}\right)^{-2} \tag{3}$$

The excitation acceleration spectrum, $G_a(\omega)$ is then obtained by differentiating twice as follows:

$$G_a(\omega) = \frac{\omega^4}{v} \cdot G_d(\Omega_o) \cdot \left(\frac{\Omega}{\Omega_o}\right)^{-2} \tag{4}$$

4.2.2. Quarter car response PDS

In the frequency domain, the quarter-car acceleration response PDS, $R_a(\omega)$ is finally obtained through the transmissibility FRF, $T(\omega)$ by:

$$R_a(\omega) = T^2(\omega)G_a(\omega) \tag{5}$$

The acceleration PDS response for the two selected quarter-car models travelling on a typical road (Class B - [34]) at 80 km/h are shown in Fig. 3. Note that, as linearity is assumed, the shape of the response PDS remains the same regardless of vehicle speed or road roughness.

4.3. Quarter-car shock response

When a quarter-car encounters a surface aberration, its response will be dependent on the frequency structure (frequency range) of the aberration relative to the FRF of the quarter car. This, of course, also depends on the speed at which the quarter-car interacts with the aberration. To complicate matters further, the shape of road surface aberrations can vary greatly hence influencing their frequency structure. A reliable and robust shock detection algorithm must be able to cope with the vehicle response caused by the great variety of road aberrations that exist on road surfaces.

4.3.1. Aberration geometry characteristics

Road surface aberrations include road damage features such as cracking, potholes, bumps and patches and surface deformation (e.

Table 2
Effect of aberration shape on frequency bandwidth.

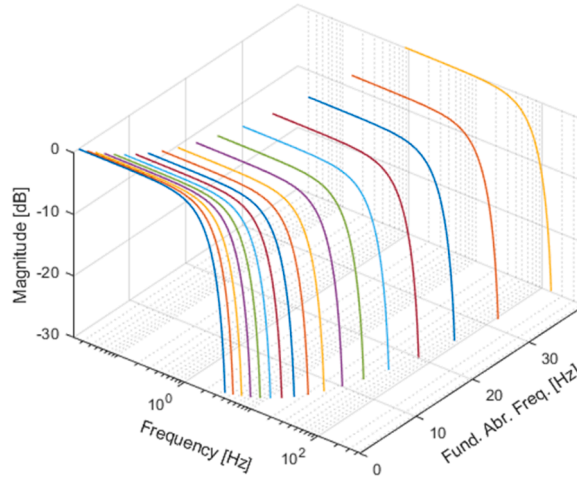| Aberration shape	Frequency bandwidth factor (f_b) (at −3.01 dB)
Half sine	1.21
Hanning	1.32
Tukey [0.8]	1.06
Synthesised aberration	1.33

Fig. 5. Frequency response of Hanning function with respect to the fundamental aberration frequency.

g. rutting) [35], as well as artificial features, such as crowned intersections, drainage inlets, utility covers, railway crossings, bridge approaches and bridge joints. Idealised models for built-in surface features such as, changes in grades at intersection [36]. camber at bridges [37] and grades for drainage [38] have been developed. Aberrations in the form of bridge expansion joints and railway crossings have also received considerable attention [39]. A study published by the National Academies of Sciences, Engineering, and Medicine [40] present typical examples of road elevation data with localised roughness and show that these are significant contributors to poor ride quality especially in urban areas. Kropáč & Múčka [41] undertook an extensive study of the shape of obstacles (bumps and potholes) and found that these were best modelled using a power function or a simple half-sine. They also tried models based on a half-ellipse with vertical slopes at the boundary as the most aggressive shape, and cosine functions with zero slope at its boundary as the smoothest shape. Overall, they show that there is significant variation in obstacle shapes and suggest that, for the range of models investigated, it not important which analytical shape is applied and that any of the shapes can be useful for simulation tasks. Given the wealth of information presented for bumps and potholes, this paper will focus on synthesized aberrations designed to represent typical bumps and potholes in the first instance. It is important to note that, in the context of this paper, linearity is assumed in the model (contact between the tyre and the road is maintained) and the polarity (potholes or bumps) of the aberration is, therefore, unimportant. Additionally, on real vehicles, sharp aberration boundaries are filtered-out by the rolling tyre. As such an effect is not included in the numerical model, functions that have smooth boundaries should be employed to define the aberration.

4.3.2. Synthesizing aberrations

In the time domain, physical aberrations can be broadly represented using the ratio of the vehicle speed and the aberration wavelength (twice the length) or wavelengths if complex. For the purpose of developing and optimising a shock detection algorithm, aberrations can be represented by simple mathematical functions such as the half-sine pulse, the Hanning (or Hann) window function and the more versatile Tuckey window function [42]. Examples of each mathematical aberration type along with a more complex synthesized aberration are presented in Fig. 4 in both the temporal and frequency domain. As seen in the results presented in Fig. 4, the aberration frequency bandwidth is mildly dependent on aberration. The variation in frequency bandwidth is listed in Table 2 as a frequency bandwidth factor, f_b.

The fundamental (Af_f) and effective (Af_e) aberration frequencies are defined respectively as:

$$Af_f = \frac{v}{2A_l} \tag{6a}$$

and
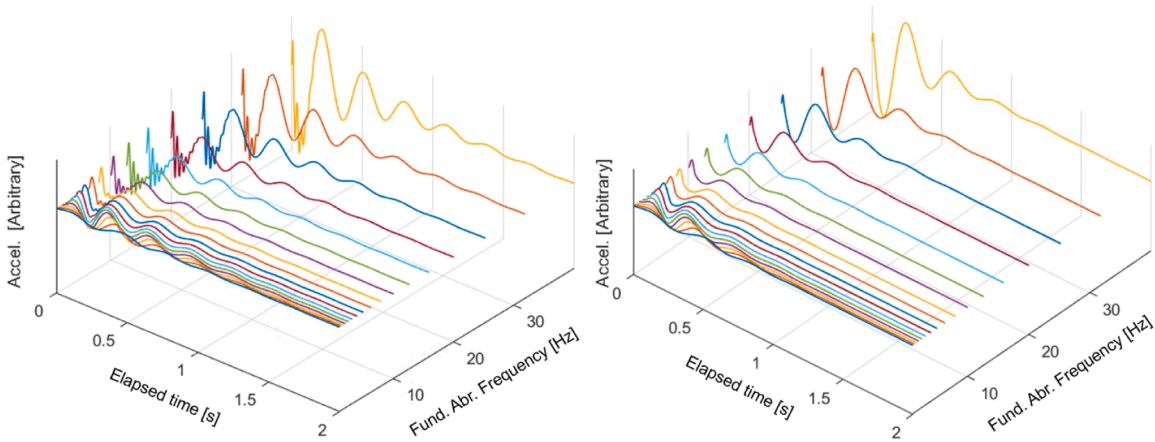
$$Af_e = f_b \cdot Af_f \tag{6b}$$

Fig. 6. Quarter-car numerical model sprung mass response to Hanning aberrations for varying fundamental aberration frequency. Left: typical air suspension [30], Right: typical steel suspension [31].

Fig. 7. Quarter-car numerical model sprung mass response to Hanning aberrations for varying fundamental aberration frequency. Left: typical air suspension [30], Right: typical steel suspension [31].
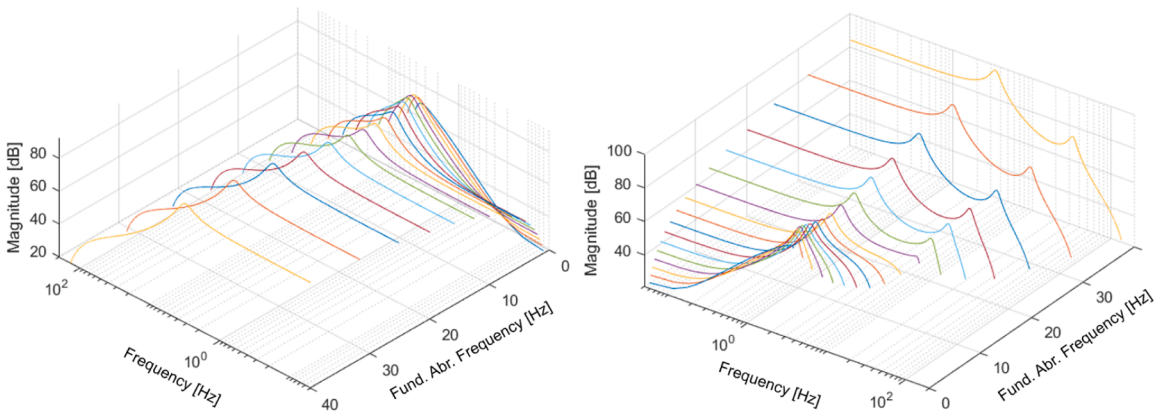
where v is the speed at which the vehicle encounters the aberration and A_l is the length of the aberration.

Notably, the excitation frequency bandwidth produced by a quarter-car increases as the fundamental aberration frequency increases (shorter aberration or higher vehicle speed) as shown in Fig. 5.

4.3.3. Quarter-car response to surface aberrations

The resulting effects on the response of a typical quarter-car model due to Hanning function shaped aberrations of lengths ranging between 0.1 and 15 m (at a simulated speed of 50 km/hr) are shown in the time domain in Fig. 6 and the corresponding frequency domain in Fig. 7. These results show that the character of the quarter-car response changes with the fundamental aberration frequency – hence the excitation bandwidth. For aberration frequency bandwidths below the second resonant mode, only the first resonant frequency is manifested in the response. As the aberration frequency bandwidth increases, the frequency component corresponding to the second (unsprung mass) resonant frequency becomes increasingly apparent. This phenomenon results in a more complex response that contains two distinct frequencies representing the two natural modes of the quarter car model. Knowing if a shock is primarily associated with either the first or second natural mode of the quarter car model is useful; not least for simulation. Consequently, the shock detection algorithm will be designed so that it distinguishes shocks that correspond to either the first or second natural mode of the quarter car model.

Under normal operating conditions, road surface aberrations are rarely as well-defined in shape as a Hanning function for example but will instead, involve more complex shapes. Nonetheless, as shown by Kropáč & Múčka [41], most aberrations are similar in overall shape to the Hanning function, and it is therefore not unreasonable to expect that responses not too dissimilar to those shown in Figs. 6 and 7 will occur.

In addition to the complexities of the vehicle's shock response to the surface aberration, when a vehicle is travelling at speed on uneven road surfaces, this response will be superimposed onto the underlying vibrations. This superposition is one of the main
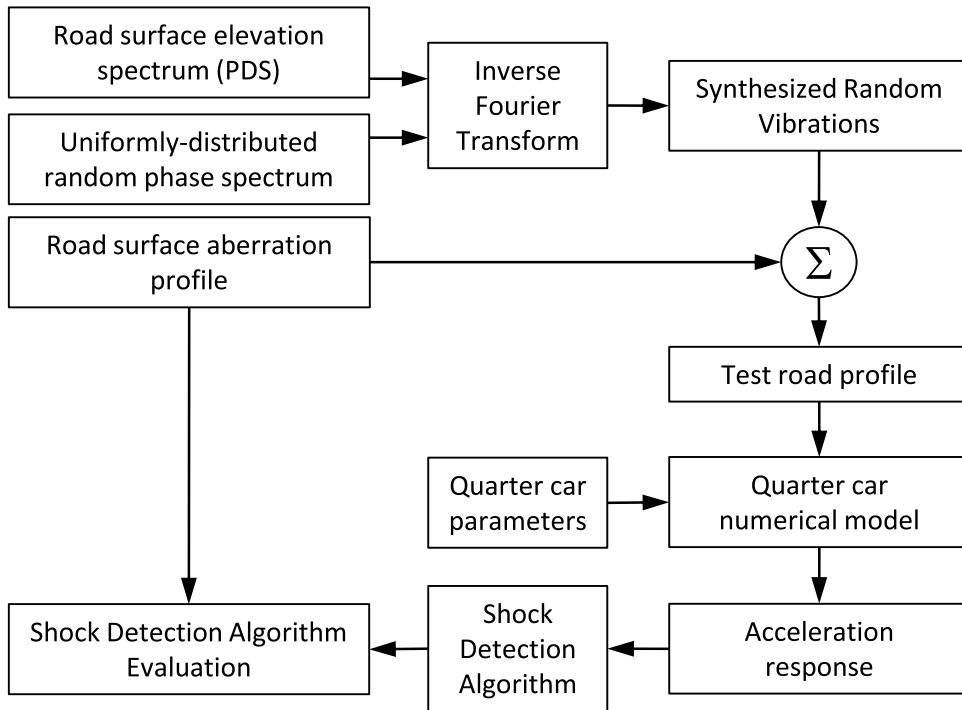
Fig. 8. Overall shock detection algorithm evaluation flowchart.

challenges to be overcome when developing a shock detection algorithm for road vehicles.

4.4. Road profile synthesis and quarter-car response

In order to evaluate the performance of any shock detection algorithm, realistic random road elevation profiles of any length and nominal roughness need to be synthesized. In this study, this was achieved using the method described by Rouillard et al. [43] and Rouillard [44] which involves combining the desired road elevation Power Spectral Density (PSD) function with a corresponding (uniformly-distributed) random phase spectrum using the inverse Fourier transform. This approach produces a random signal that conforms to the Gaussian distribution in accordance with the central limit theorem. There exists a number of models for the elevation PSD function, but it is broadly accepted that the model published in ISO-8608 (Eqn. (2)) represents observed elevation spectra reasonably well.

Following the synthesis of the random elevation profile, a surface aberration profile, containing a sequence of aberrations of predetermined lengths, amplitudes and locations is produced. For this paper, the aberration shapes were generated using the Hanning function. The aberration profile was then superimposed onto the synthesized random elevation profile to produce the 'test' profile. The 'test profile' is then used to compute the vibration response of any quarter-car model travelling at a pre-determined speed. The resulting response is submitted to the shock detection algorithm for evaluation by counting true and false detection rates. The overall approach to evaluating the performance of the shock detection algorithm is shown in Fig. 8.

5. Shock detection algorithm

In developing a shock detection algorithm, the following are taken into consideration:

- Detection sensitivity (ratio of true positive: all detected shocks) is more important for large shocks (i.e. missed-detection of large shocks should be minimised).
- The quarter-car response is a function of the effective aberration frequency.
- The algorithm should be as objective (automated) as possible with little or no subjective user input required.

Basic definitions:

- *NAS*: Number of actual (known) shocks
- *NDS*: Number of shocks detected by the algorithm
- *TP*: Number of True Positives (when detected shock coincides with known shock)
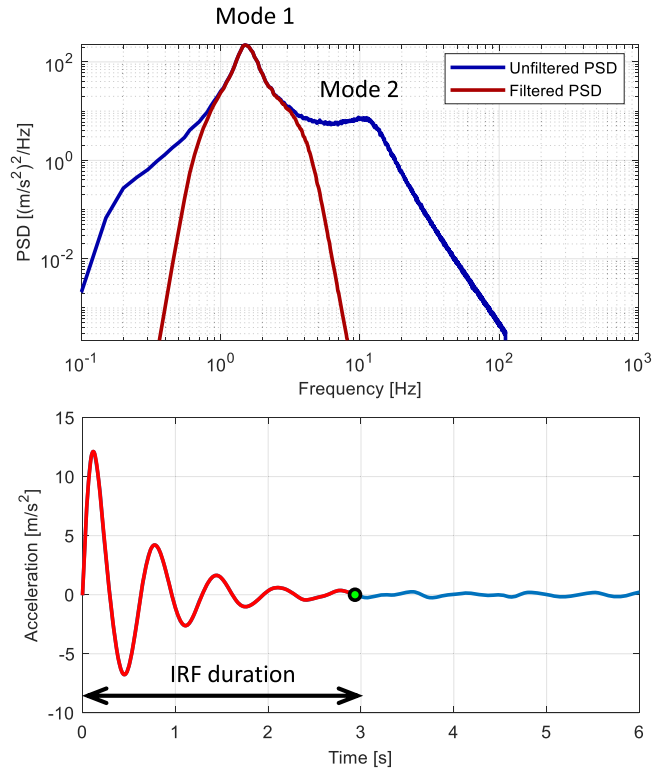
Fig. 9. Sprung-mass (first) resonant mode impulse response function.

- *FP*: Number of False Positives
- *FN*: Number of False Negatives
- *TN*: Number of True Negatives (not used in this context)
- *Se*: Sensitivity
- *Sp*: Specificity (mot used in this context. Needs *TN* to compute)
- *FDR*: False Detection Ratio
- *TDR*: True Detection Ratio

$$FP = NDS - TP \tag{7a}$$

$$FN = NAS - TP \tag{7b}$$

$$Se = \frac{TP}{(FN + TP)} \tag{7c}$$

$$FDR = \frac{FP}{(TP + FP + FN)} \tag{7d}$$

$$TDR = 1 - FDR = \frac{NAS}{(NAS + NDS - TP)} \tag{7e}$$

Given the relative importance of large shocks compared to smaller shocks, the shock detection algorithm will be optimized, and its performance evaluated based on a sufficiently high *TDR*. The broad approach proposed for the automated detection of shocks from road vehicle vibration response data is as follows:

(1) The average Power Density Spectrum (PDS) of the acceleration response signal is calculated using an appropriate frequency resolution and ensemble averaging [7] to reveal the resonance frequency bands which, for a quarter-car vehicle, corresponds to the sprung and unsprung mass natural frequencies.
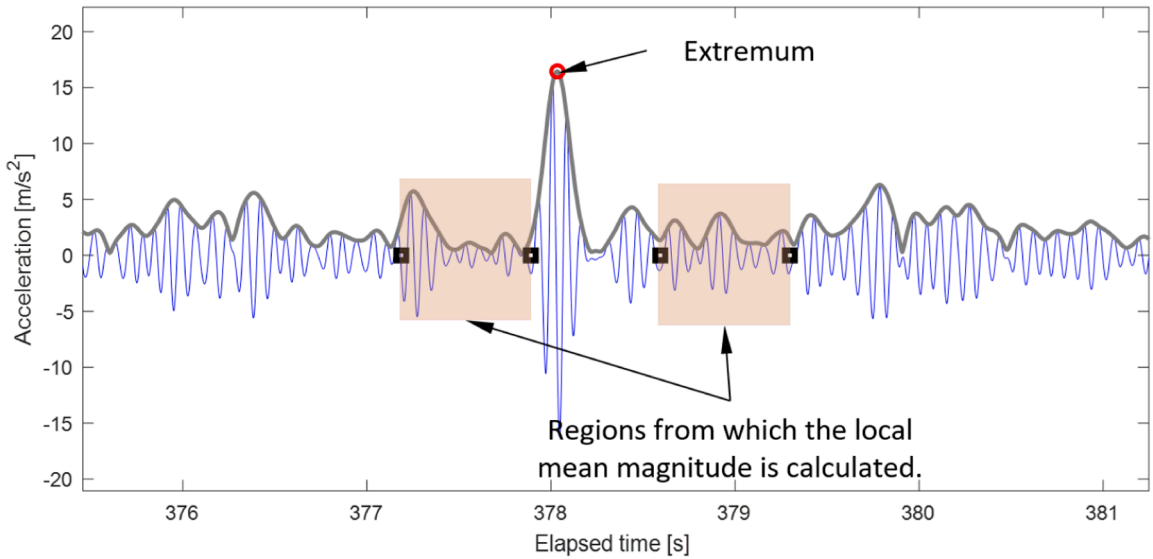
Fig. 10. Method for calculating the local mean hence the local peak-to-mean ratio.

(2) The acceleration response signal is filtered within a frequency band of interest around one of the identifiable resonances (spectral peak) on the average PDS using an appropriate FIR filter (i.e. Butterworth) of appropriate order (Fig. 9).

(3) The vehicle's impulse response (IR) function is calculated (extracted) from the band-pass filtered response vibration signal using the Random Decrement technique [45,46] and is used to determine the duration of the data analysis window (Fig. 9).

(4) The instantaneous magnitude (envelope) of the filtered signal is computed by means of the Hilbert Transform [47].

(5) The Hilbert magnitude signal is scanned for extrema (peaks) which are then used to calculate the local peak-to-mean ratio (LPTMR). This scan is achieved by calculating the ratio of the extremum to the local mean Hilbert magnitude in the vicinity (on either side) of the extremum as illustrated in Fig. 10.

(6) The LPTMR then is checked against a user-specified detection threshold and is used as an indicator for the presence of shocks in the signal.

The algorithm requires the setting of three important parameters: 1) the cut-off frequencies of the band-filters used to isolate each mode; 2) the duration of the window over which the local mean magnitude is calculated and 3) a detection threshold to maximize the true detection ratio (TDR) and minimise false positives.

5.1. Mode separation frequency filter

A fourth order Butterworth band-pass filter was applied to the acceleration response signal to isolate each of the two resonant frequencies such that the impulse response function (IRF) (calculated using the random decrement technique) exhibited a single dominant frequency, and its duration could be estimated as shown in Fig. 9 for mode 1 of sample data set.

5.2. Calculating the instantaneous magnitude and the local peak-to-mean ratio

The instantaneous magnitude of the filtered signal, $x(t)$, is computed using the Hilbert transform which is formally defined by Eq. (8)

$$H(x(t)) = \lim_{\varepsilon \to \infty} \frac{1}{\pi} \int\limits_{|s-t|>\varepsilon} \frac{x(s)}{t-s}\, ds \qquad (8)$$

Nowadays, the Hilbert transform [48] is efficiently calculated on sampled signals by using the FFT, applying a phase shift to the phase of the signal and returning to the time domain via the Inverse FFT [49]. The resulting analytic (complex) signal is then used to compute the instantaneous magnitude of the signal [49].

The mean in the vicinity of any detected magnitude extremum (the local mean) is calculated across two segments of the signal - one on either side of the detected extremum as shown in Fig. 10. Repeated experiments have shown that the most consistent results were obtained when the duration of these segments and that of the separation segment corresponded to twice the IRF duration.
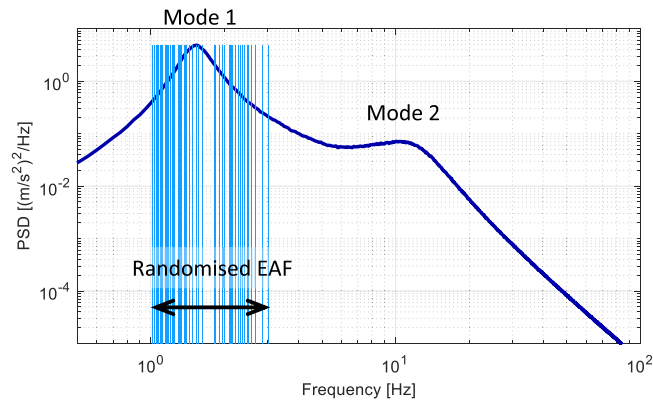
Fig. 11. Random effective aberration frequencies (EAF) across mode 1 resonant frequency band for the Cebon quarter-car model.
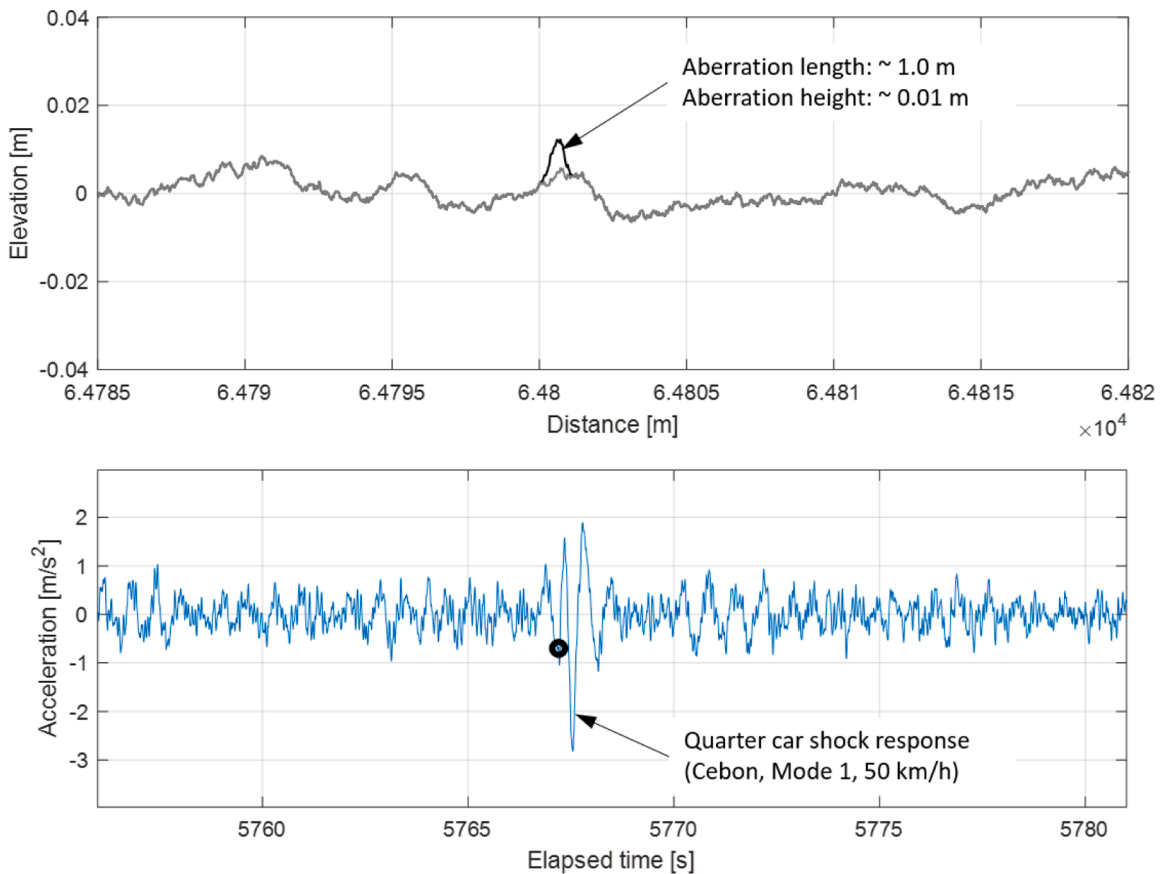

Fig. 12. Artificial generation of aberrations onto random road elevation profile (top) along with corresponding quarter-car acceleration response (bottom) for a typical case.

5.3. Detection threshold

The sole parameter that needed to be set to establish if the magnitude of an event (based on its LPTMR) is sufficiently large to be considered as a shock, is the detection threshold. The optimum LPTMR threshold was determined experimentally by synthesizing random road elevation signals (as per Fig. 8) that were laced with surface aberrations at known regular intervals. The aberrations shape was of the Hanning type with (uniformly) randomized wavelengths across the frequency range for each mode corresponding to the quarter car models used as illustrated in Fig. 11. The amplitude of the aberrations were also randomized in accordance with the statistical model by Kropáč & Múčka [50] whereby the aspect ratio (length:height) of road surface aberrations were found to conform

11

Table 3
Road roughness classification used to synthesize test road profiles.

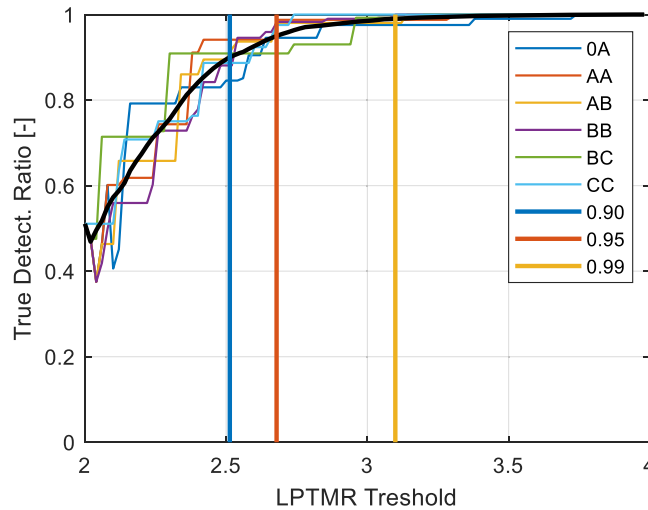| Roughness Class	ISO Roughness Class	$G_d(\Omega_o)$ [10^{-6} m³/rad] Mean
0A	–	0.5
AA	A (mean)	1.0
AB	A (upper)	2.0
BB	B (mean)	4.0
BC	B (upper)	8.0
CC	C (mean)	16.0

Fig. 13. TDR as a function of local peak-to-mean ratio threshold for a typical case (DePont quarter-car model, mode 2, 80 km/hr).

Table 4
Summary of detection threshold optimisation.

TDR	Detection Threshold (local PTM ratio)	
	Mean	CoV [%]
0.90	2.7	10
0.95	3.0	8
0.99	3.4	11

with the Gaussian distribution with a mean, μ, and standard deviation, σ, of 161 and 51.9 respectively. In addition, Kropáč's & Múčka's statistical model limited the aspect ratio to a maximum of 333.3 ($\mu + 3.3\sigma$) and a minimum of 14 (μ - 2.8σ) with an absolute lower height limit of 3 mm.

For each 'test road profile' 400 shocks were superimposed on a 120 km long synthesized road, an example superimposed aberration and resulting vibration response is shown in Fig. 12. In total, 72 such 'test road profiles' were created to accommodate six road roughness levels. The roughness of modern road networks rarely exceeds ISO class C [51]. In order to enable the evaluation of road roughness on the proposed shock detection algorithm, alternative, finer increments in mean roughness (similar to the scheme proposed by Lamb & Rouillard [52]), than those listed in ISO-8608 have been used and are shown in Table 3. Test roads of varying roughness levels were used in order to find the limit where the aberrations are overwhelmed by the inherent roughness of the road and where the severity of the response from the aberration becomes small compared to the underlying vibration response.

The test road profiles were used to excite the two-representative quarter-car models (Cebon for typical air suspension and DePont for typical steel suspension) for two resonant modes: sprung mass and unsprung mass (axle hop) frequencies and three vehicle speeds (20, 50 and 80 km/hr). The resulting acceleration response signals that were then submitted to the shock detection algorithm.

The shock detection algorithm was set to repeatedly analyse all 72 aberration-laced 120 km-long roads with the LPTMR threshold set to vary between 2 and 4 in intervals of 0.1 in order to determine the optimum detection threshold. For each case, the True Detection Ratio, TDR, (Eq. (7e)) was computed – typical case shown in Fig. 13– yielding, for all 72 scenarios, the summary overall detection threshold shown in Table 4. These results indicate that the detection threshold is largely independent of vehicle type, vehicle speed, resonant mode and road roughness.
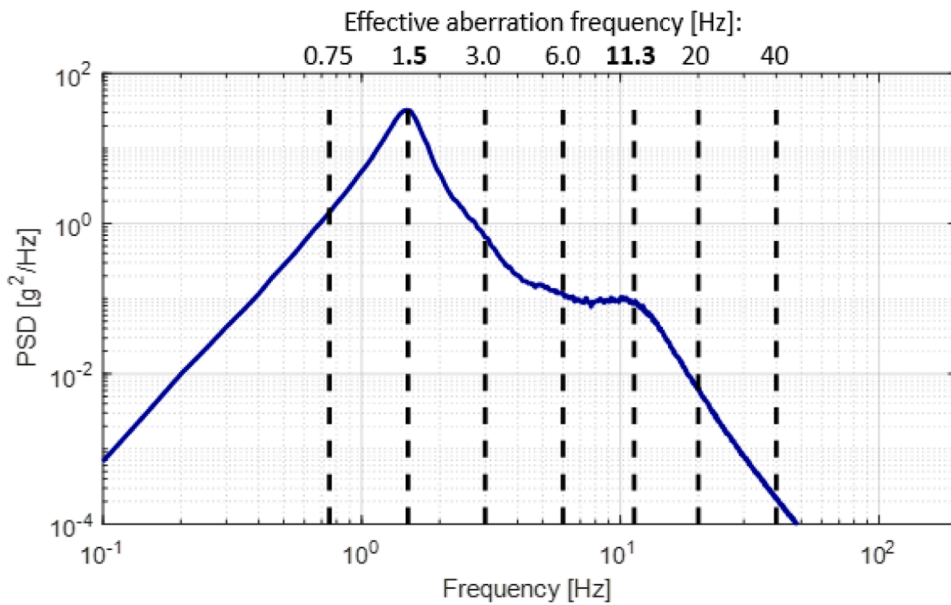
Fig. 14. Effective aberration frequencies of artificially-generated shocks for the Cebon quarter-car model with resonant frequencies at 1.5 and 11.3 Hz.

6. Shock detection performance

In order to determine the effectiveness and the performance limits of the shock detection algorithm, road surface aberrations of pre-determined lengths and decreasing heights were generated and superimposed on synthesized random road profiles of varying nominal roughness levels. This was aimed at establishing how the response from road surface aberrations of varying effective frequencies are attributed to the two modes; that is, detected shocks are assigned to either first or second mode depending on their frequency structure. However, because the frequency content of an aberration extends well outside the effective aberration frequency (Figs. 4 and 5), it is expected that, in practice, aberrations with effective frequencies away from the frequency of the selected mode will still generate responses falling inside the filter pass band around the selected mode.

The aberration-laced road profiles were used to calculate the acceleration response of the two-representative quarter-car models (namely Cebon for air suspension and DePont for steel leaf suspension) for a range of typical vehicle speeds. The aberration lengths were set so that their effective frequencies were evenly spread across the range of response frequencies of each quarter-car model/speed combination making sure that two aberration lengths coincided with the resonant frequencies as illustrated in Fig. 14. For each aberration length, nine aberrations were created with decreasing heights from a minimum aspect (length:height) ratio of 13 to a maximum of 333.3 with an absolute lower height limit of 3 mm as defined by Kropáč & Múčka [50]. These were set to establish the smallest aberration detectable by the algorithm for a range of vehicle speeds and road roughness levels. The resulting aberration amplitudes, wavelengths and effective frequencies are shown for both the Cebon and DePont quarter-car models in Fig. 15.

The acceleration response for each scenario (vehicle type, speed and road roughness) was subjected to the shock detection algorithm to determine which of the shocks were correctly detected (true positives) and any false positives.

7. Results

The shock detection algorithm was evaluated for a broad range of scenarios namely two vehicle models, three vehicle speeds (20, 50 and 80 km/h) and six road classes (0A to CC). Results from the shock detection algorithm – with the LPTMR threshold set at 3.4 (target TDR of 0.99) are shown for typical cases in Fig. 16 for the air ride suspension (Cebon model) and in Fig. 17 for steel suspension (DePont model). These graphs show detected shocks with each segment (separated by red lines) corresponding to surface aberrations of varying effective frequencies and aberration lengths as denoted on the graph. The results demonstrate the effectiveness of the shock detection algorithm which, in the main is more effective for air ride suspension (Cebon quarter-car model). Overall, all shocks with LPTMR values above the set threshold of 3.4 were detected with no false positives identified. This may well be due to the absence of spurious events (noise) when undertaking numerical simulations. It would not be unreasonable to expect some detection of false positives from physical experiments.

Fig. 16 shows how shocks with frequencies in the vicinity of the two natural modes (1.51 and 11.3 Hz) are separated into their respective modes (1 and 2) thereby distinguishing the type of shock detected. Unsurprisingly, large shocks (those with LPTMR values well in excess of the threshold of 3.4) are easily and reliably detected especially when the underlying road roughness is low (class AA). As the underlying road roughness increases, the transient acceleration response (shocks) resulting from the aberrations becomes less
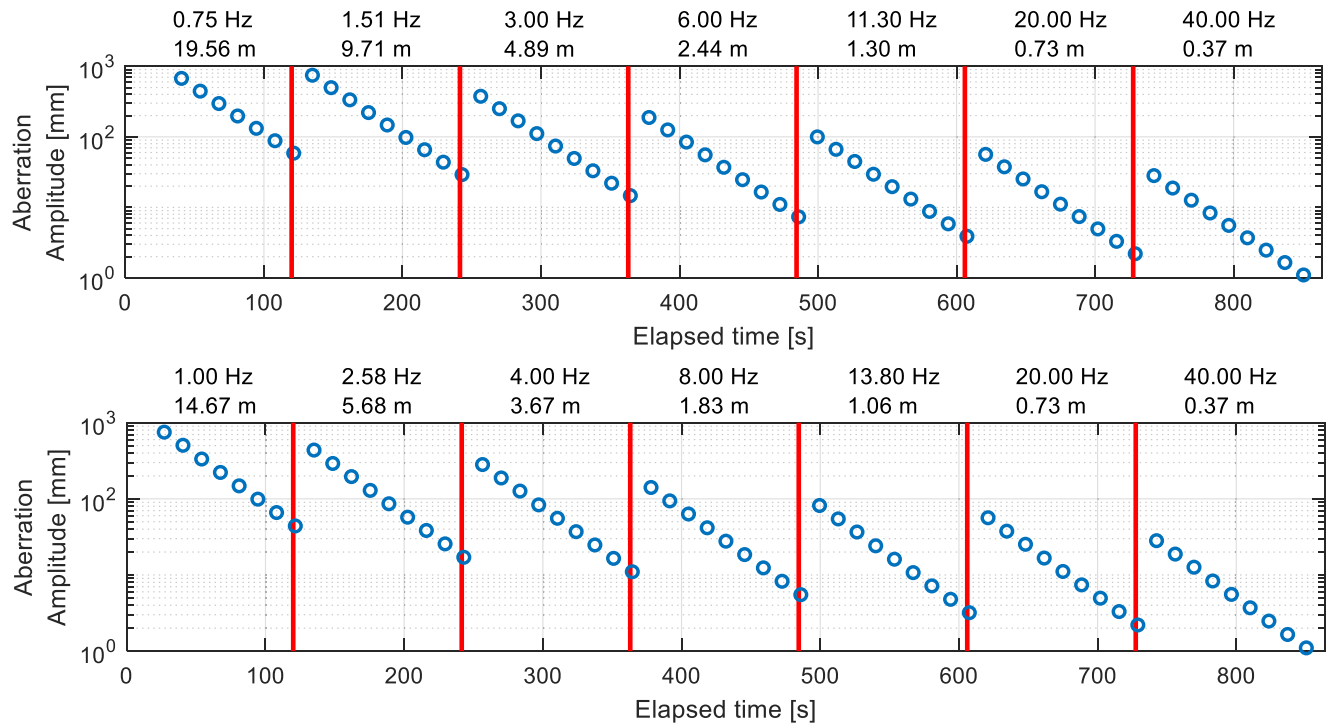
Fig. 15. Aberration amplitudes, effective frequencies and wavelengths for the Cebon (top) and DePont (bottom) models at 80 km/h used to validate the shock detection algorithm.

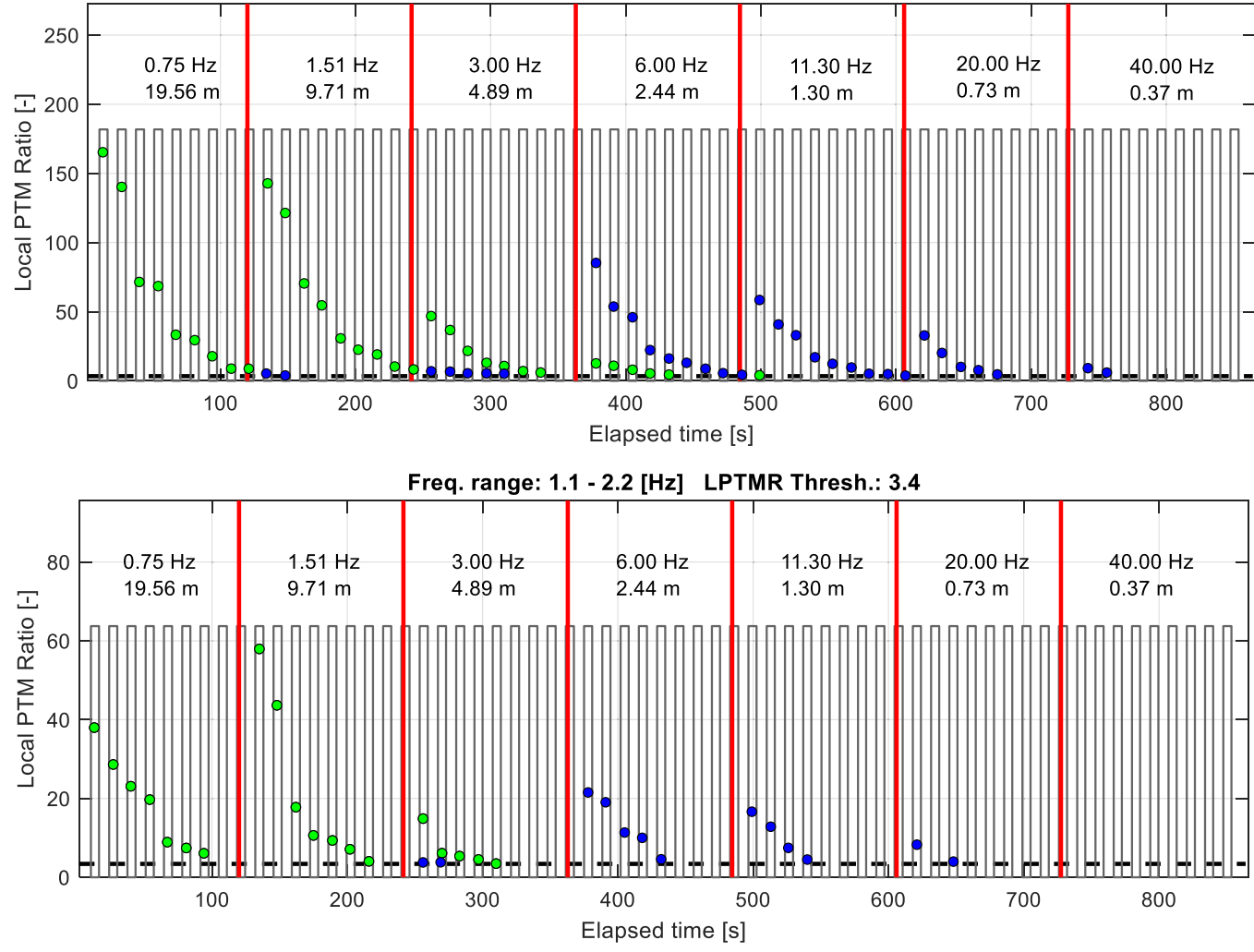**Fig. 16.** Detected shocks for Cebon quarter-car model at 80 km/h on class AA road (top) and class CC road (bottom). Green: detected mode 1 shocks; Blue: detected mode 2 shocks. Grey bins: shock locations. Dashed black line: LPTMR threshold (3.4).
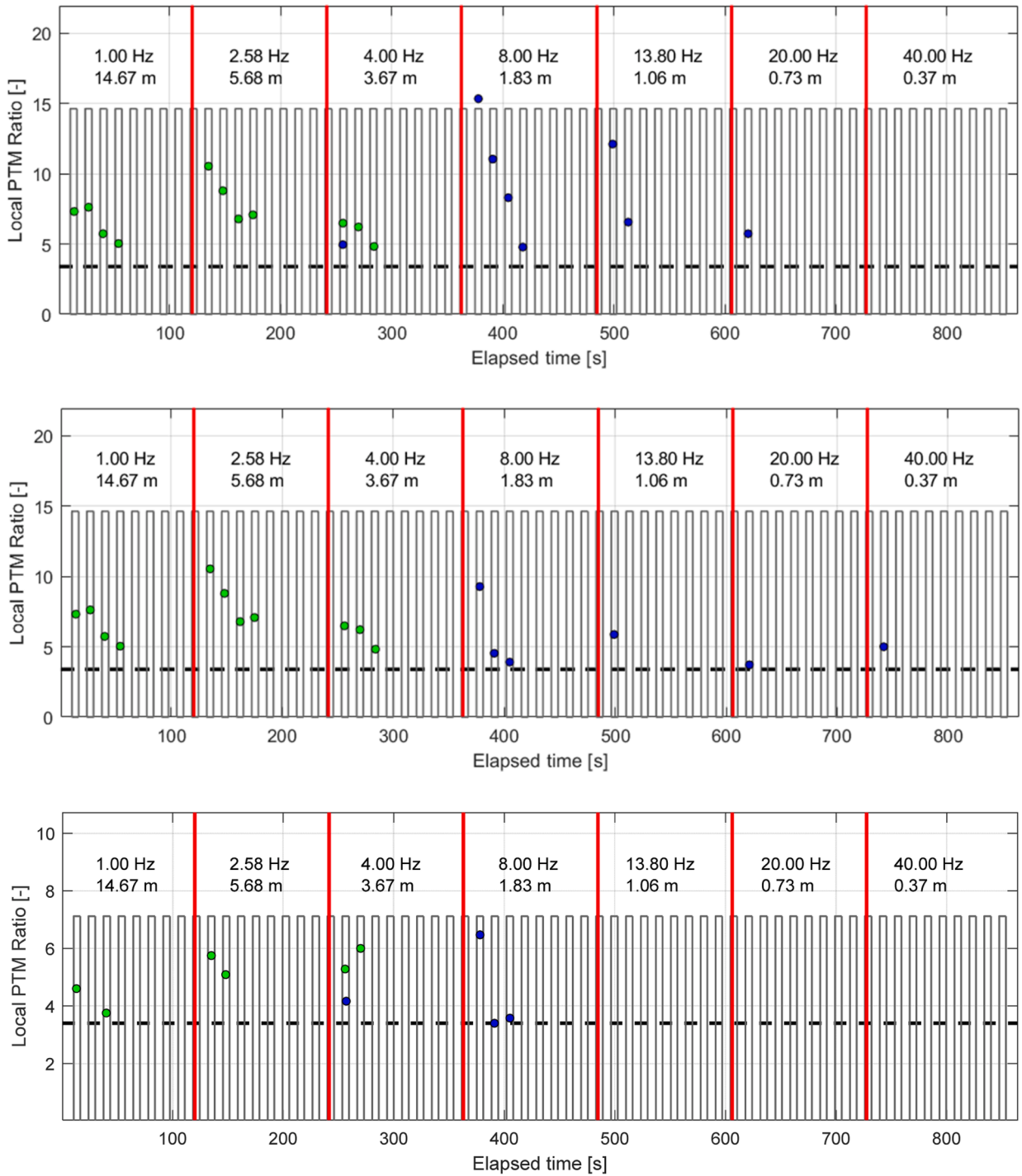
Fig. 17. Detected shocks for DePont quarter-car model at 80 km/h on (from top to bottom) class AA, BB and BC roads. Green: detected mode 1 shocks; Blue: detected mode 2 shocks. Grey bins: shock locations. Dashed black line: LPTMR threshold (3.4).

distinct from the background vibrations and therefore more difficult to detect as is the case for class CC roads in this example.

Detection of shocks in the case of steel suspension (DePont quarter-car model) is less effective (Fig. 17) due to the higher overall vibration response (see Fig. 3) which tends to drown-out transient acceleration responses from smaller road surface aberrations and the relatively low damping for the first mode which produce a strong and persistent narrow band response at the first resonant mode.
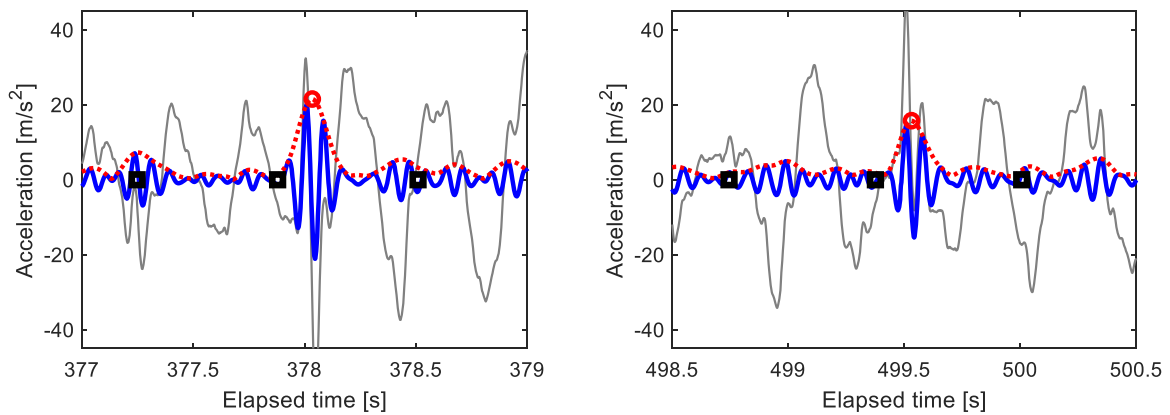
Fig. 18. Illustration of detection of shocks from aberration of different effective frequencies - left: 8.0 Hz, right: 13.8 Hz - for mode 2 (13.8 Hz in this case). Grey line: Raw (unfiltered) signal; Blue: band-pass filtered signal; Red: Hilbert envelope; Black symbols: range to establish local mean magnitude.

It is interesting to note that, in some cases, the algorithm detected higher LPTMR second mode shocks from effective aberration frequencies adjacent to the selected mode as is the case for roads class BB and BC. This is the result of the complexities associated with combining randomly located shocks onto a random road profile as well as the complex interaction between the 2DoF systems and the random surface profile at different frequency bands. This is illustrated in Fig. 18 which shows how the level of vibration response in the filtered band (in this case around 13.8 Hz) adjacent to the shock influences the LPTMR. The left-hand graph reveals the low vibration magnitude on either side of the detected shock resulted in a high LPTMR value whereas, in the right-hand graph, the background vibration magnitude is relatively higher resulting in a lower LPTMR value.

8. Conclusion

The first stages in the development and optimisation of a shock detection algorithm from the vibration response of road vehicles have yielded positive results. The ability of the shock detection algorithm to attribute shocks to one of the two natural frequencies of the 2DoF quarter car model was found to be reliable. Sensitivity analysis was undertaken to establish the optimum LPTMR threshold and was found to be 3.4 for a TDR of 0.99. Validation was undertaken on artificially-generated roads of varying roughness onto which aberrations of varying length (effective frequencies) and diminishing amplitudes were superimposed. Results show that shocks of 'significant' magnitudes – that is those with LPTMR of 3.4 and above - are always detected with no detection of false positives. As the road roughness increases relative to the aberration amplitudes, the resulting shocks become increasingly drowned-out by the vibration response due to the underlying road roughness especially for the quarter-car model with steel suspension. The main conclusion is that the signal analysis approach taken is ultimately effective based on the numerical modelling undertaken. However, it needs to be validated for more realistic conditions using measured vibration response data from physical vehicles first under controlled conditions then during normal, in-service conditions. It is suggested that this be first achieved by using a physical quarter-car vehicle on a road simulator; second by using the same physical quarter-car vehicle on a test track onto which known aberrations are affixed and finally, on a 'real', multi-wheeled vehicle on the same test track. The latter will pose significant challenges as it is expected that the response of multi-wheeled vehicles when encountering road surface aberrations will be more complex than those produced by a single-wheeled vehicle. Finally, direct comparison of performance of the proposed method against alternative approaches would be a valuable exercise and make for interesting further research.

Declaration of Competing Interest

The authors declare the following financial interests/personal relationships which may be considered as potential competing interests

Vincent Rouillard reports was provided by Victoria University. Vincent Rouillard reports a relationship with Victoria University that includes: employment.

Data availability

No data was used for the research described in the article.

References

[1] Z.W. Wang, K. Fang, Dynamic performance of stacked packaging units, Packag. Technol. Sci. 29 (10) (2016) 491–511.

[2] K. Fang, Z.W. Wang, The statistical characteristics of maxima of contact force in stacked packaging units under random vibration, Packag. Technol. Sci. 31 (5) (2018) 261–276.

[3] K. Fang, Z.W. Wang, Influence of jumping phenomenon on response of package under random vibration, Packag. Technol. Sci. 31 (9) (2018) 585–599.

[4] C. Liu, X. Deng, J. Liu, Z. Zheng, Impact-induced nonlinear damped vibration of fabric membrane structure: theory, analysis, experiment and parametric study, Composit. Part B: Eng. 159 (2019) 389–404.

[5] F. Ostrem, W.D Godshall, An Assessment of the Common Carrier Shipping Environment, 22, Department of Agriculture, Forest Service, Forest Products Laboratory, 1979.

[6] A.G. Piersol, T.L. Paez, Harris' Shock and Vibration Handbook, McGraw-Hill Education, 2010.

[7] J.S. Bendat, A.G. Piersol, Random data: Analysis and Measurement Procedures, John Wiley & Sons, 2011.

[8] K. Ogata, Discrete-time Control Systems, Prentice-Hall, Inc, 1995.

[9] J. Lepine, V. Rouillard, M. Sek, Review paper on road vehicle vibration simulation for packaging testing purposes, Packag. Technol. Sci. 28 (8) (2015) 672–682.

[10] V. Rouillard, M.J. Lamb, J. Lepine, M. Long, D. Ainalis, The case for reviewing laboratory-based road transport simulations for packaging optimisation, Packag. Technol. Sci. 34 (6) (2021) 339–351.

[11] B. Bruscella, Doctoral dissertation, Victoria University of Technology, 1997.

[12] V. Rouillard, M.A. Sek, The use of intrinsic mode functions to characterize shock and vibration in the distribution environment, Packag. Technol. Sci.: Int. J. 18 (1) (2005) 39–51.

[13] V. Rouillard, R. Richmond, A novel approach to analysing and simulating railcar shock and vibrations, Packag. Technol. Sci.: Int. J. 20 (1) (2007) 17–26.

[14] J. Lepine, V. Rouillard, M. Sek, Wavelet transform to index road vehicle vibration mixed mode signals, in: Noise Control and Acoustics Division Conference 56819, American Society of Mechanical Engineers, 2015.

[15] D. Nei, N. Nakamura, P. Roy, T. Orikasa, Y. Ishikawa, H. Kitazawa, T. Shiina, Wavelet analysis of shock and vibration on the truck bed, Packag. Technol. Sci.: Int. J. 21 (8) (2008) 491–499.

[16] L. Wei, T.F. Fwa, Z. Zhe, Wavelet analysis and interpretation of road roughness, J. Transp. Eng. 131 (2) (2005) 120–130.

[17] A.Y. Ayenu-Prah, N.O. Attoh-Okine, Comparative study of Hilbert–Huang transform, Fourier transform and wavelet transform in pavement profile analysis, Veh. Syst. Dyn. 47 (4) (2009) 437–456.

[18] J. Lepine, V. Rouillard, M. Sek, Using the Hilbert-Huang transform to identify harmonics and transients within random signals, in: 8th Australasian Congress on Applied Mechanics: ACAM 8: ACAM 8, Barton, ACT, Engineers Australia, 2014, pp. 157–166.

[19] Z. Wu, N.E. Huang, A study of the characteristics of white noise using the empirical mode decomposition method, in: Proceedings of the Royal Society of London. Series A: Mathematical, Physical and Engineering Sciences 460, 2004, pp. 1597–1611.

[20] J. Lepine, Doctoral dissertation, Victoria University, 2016.

[21] A. Mednis, G. Strazdins, R. Zviedris, G. Kanonirs, L. Selavo, Real time pothole detection using android smartphones with accelerometers, in: 2011 International conference on distributed computing in sensor systems and workshops (DCOSS), IEEE, 2011, pp. 1–6.

[22] A. Basavaraju, J. Du, F. Zhou, J. Ji, A machine learning approach to road surface anomaly assessment using smartphone sensors, IEEE Sens. J. 20 (5) (2019) 2635–2647.

[23] W. Chao, Z. Wang, S. Hu, J. Lepine, X. Na, D. Ainalis, M. Stettler, An automated machine-learning approach for road pothole detection using smartphone sensor data, Sensors 20 (19) (2020) 5564.

[24] D.C. Knox, Doctoral dissertation, 2018.

[25] F. Wirthmueller, J. Hipp, K.U. Sattler, M. Reichert, CPD: crowd-based pothole detection. VEHITS, 2019, pp. 33–42.

[26] C. Altmann, J. Ferris, Theoretical development of localized pseudo damage, SAE Int. J. Passeng. Car.-Mech. Syst. 13 (2020) 21–30.

[27] C. Altmann, J. Ferris, Identification of damaging road events using pseudo damage density, SAE Int. J. Passeng. Car.-Mech. Syst. 13 (2020) 125–134.

[28] C. Altmann, J. Ferris, Similarity between damaging events using pseudo damage density, SAE Int. J. Passeng. Car.-Mech. Syst. 13 (2020) 207–224.

[29] K.B. Todd, B.T. Kulakowski, Simple computer models for predicting ride quality and pavement loading for heavy trucks, Transp. Res. Rec. 1215 (1989) 137–150.

[30] D. Cebon, Handbook of Vehicle-Road Interaction, Swets & Zeitlinger, 1999.

[31] J. De Pont, Road Profile Characterisation, Transit New Zealand, 1994.

[32] A.N. Heath, Application of the isotropic road roughness assumption, J. Sound Vib. 115 (1) (1987) 131–144.

[33] H. Prem, Road roughness influence on suspension performance, in: SYMPOSIUM ON HEAVY VEHICLE SUSPENSION, 1988.

[34] ISO, Mechanical Vibration — Road Surface Profiles — Reporting of Measured Data, 2016.

[35] J.S. Miller, W.Y. Bellinger, *Distress Identification Manual for the Long-Term Pavement Performance Program* (No. FHWA-RD-03-031), Federal Highway Administration. Office of Infrastructure Research and Development, United States, 2003.

[36] K. Movassaghi, J. Lee, A. Kumat, *Roughness Analysis of Grade Breaks at Intersections* (No. FHWA/LA-93/257), Louisiana Transportation Research Center, 1993.

[37] K.K. McGhee, Smoothness provision for bridge decks, Transp. Res. Rec. 1813 (1) (2002) 210–217.

[38] A. Reggin, A. Shalaby, R. Emanuels, G. Michel, Urban considerations for using road roughness to manage road networks, in: 7th international conference on managing pavement assets, 2008, p. 8.

[39] J.M. Lima, J. de Brito, Inspection survey of 150 expansion joints in road bridges, Eng. Struct. 31 (5) (2009) 1077–1084.

[40] National Academies of Sciences, Engineering, and Medicine, Measuring, Characterizing, and Reporting Pavement Roughness of Low-Speed and Urban Roads, The National Academies Press, Washington, DC, 2019, https://doi.org/10.17226/25563.

[41] O. Kropáč, P. Múčka, Shapes of obstacles in the longitudinal road profile, Shock Vibr. 18 (5) (2009) 671–682.

[42] R.B. Blackman, J.W. Tukey, Particular pairs of windows. The Measurement of Power Spectra, from the Point of View of Communications Engineering, 1959, pp. 98–99.

[43] V. Rouillard, M.A. Sek, B. Bruscella, Simulation of road surface profiles, J. Transp. Eng. 127 (3) (2001) 247–253.

[44] V. Rouillard, Doctoral dissertation, Ph. D Thesis, Monash University, Melbourne, Australia, 2006.

[45] H.A Cole Jr, On-the-line analysis of random vibrations, in: In 9th *Structural Dynamics and Materials Conference*, 1968, p. 288.

[46] H.A Cole Jr, On-Line Failure Detection and Damping Measurement of Aerospace Structures by Random Decrement Signatures, 1973 (No. NASA-CR-2205) NASA.

[47] V. Cizek, Discrete hilbert transform, IEEE Trans. Audio Electroacoust. 18 (4) (1970) 340–343.

[48] S.C. Kak, The discrete Hilbert transform, Proc. IEEE 58 (4) (1970) 585–586.

[49] N. Thrane, The hilbert transform. B&K Technical Rewiew, 1984, p. 3.

[50] O. Kropáč, P. Múčka, Specification of obstacles in the longitudinal road profile by median filtering, J. Transp. Eng. 137 (3) (2011) 214–226.

[51] P. Múčka, International Roughness Index specifications around the world, Road Mater. Pavem. Des. 18 (4) (2017) 929–965.

[52] M.J. Lamb, V. Rouillard, Synthesizing dual-track road elevation data, Probab. Eng. Mech. 66 (2021), 103168.